Research Square

Preprints are preliminary reports that have not undergone peer review.
They should not be considered conclusive, used to inform clinical practice,
or referenced by the media as validated information.

InSAR constraints on spatiotemporal changes in plate coupling beneath Shikoku along the Nankai subduction zone

Kohei Shimotsuma

s2430132@u.tsukuba.ac.jp

University of Tsukuba: Tsukuba Daigaku https://orcid.org/0009-0004-8934-0753

Yohei Kinoshita

University of Tsukuba: Tsukuba Daigaku

Suguru Yabe

National Institute of Advanced Industrial Science and Technology Geological Survey of Japan: Sangyo Gijutsu Sogo Kenkyujo Chishitsu Chosa Sogo Center

Tadafumi Ochi

National Institute of Advanced Industrial Science and Technology Geological Survey of Japan: Sangyo Gijutsu Sogo Kenkyujo Chishitsu Chosa Sogo Center

Research Article

Keywords: Nankai subduction zone, plate coupling, InSAR

Posted Date: October 30th, 2026

DOI: https://doi.org/10.21203/rs.3.rs-11263913/v1

License: This work is licensed under a Creative Commons Attribution 4.0 International License.
Read Full License

Abstract

Estimating spatiotemporal changes in plate coupling is important for understanding the nucleation processes of megathrust earthquakes. Using Global Navigation Satellite System (GNSS) and Interferometric Synthetic Aperture Radar (InSAR) observations, we obtained crustal deformation around Shikoku, southwest Japan, from 2014 to 2025. We estimated slip deficit distributions along the Nankai subduction zone using kinematic fault slip inversions based on GNSS, InSAR, and GNSS-InSAR joint observations. Both the GNSS- and InSAR-based slip deficit models showed that slip deficit rates beneath central Shikoku decreased by up to 41 mm/year after 2019 relative to 2014–2018. We interpret this as a weakening of plate coupling rather than a long-term slow slip event, because the estimated slip deficit rates were not significantly negative even after 2019. Our results demonstrate that InSAR-derived velocities, which are sensitive to vertical displacements, can independently constrain broad-scale changes in plate coupling beneath inland regions, although they do not drastically improve the spatial resolution of plate coupling estimates. These findings suggest that InSAR observations provide valuable information on plate coupling changes, particularly in subduction zones where dense GNSS observations are unavailable.

1. Introduction

Coupled regions along subducting plates accumulate stress in the surrounding crust during the interseismic period and release it through devastating ruptures. In addition, spatiotemporal changes in plate coupling along a seismogenic zone can perturb the stress distribution at the plate interface, potentially triggering megathrust earthquakes (Segall and Bradley 2012). Geodetic and seismic observations have suggested that a decadal-scale acceleration of slip (weakening of coupling) continued downdip of the seismogenic zone until the 2011 (M_w 9.0) Tohoku-oki earthquake occurred (Mavrommatis et al. 2014, 2015). Quantifying spatiotemporal changes in plate coupling is therefore important for understanding the nucleation processes of megathrust earthquakes.

Recent advances in satellite geodetic observations, including the Global Navigation Satellite System (GNSS) and Interferometric Synthetic Aperture Radar (InSAR), have enabled continuous monitoring of crustal deformation, which reflects slip and coupling on subsurface faults. High-frequency and long-term GNSS observations provide accurate three-dimensional displacement time series. Thus, GNSS observations have played a central role in detecting subtle interseismic crustal deformation and estimating plate coupling (Nishimura et al. 2018; Plata-Martinez et al. 2024). However, GNSS observations require ground-based receivers, and not every subduction zone is covered by a dense GNSS network. In contrast, InSAR does not require ground-based receivers and provides high-spatial-resolution line-of-sight (LOS) displacement fields. Although the temporal resolution of Synthetic Aperture Radar (SAR) observations remains lower than that of GNSS, recent advances in SAR satellite missions and InSAR processing techniques have enabled the detection of subtle displacement rates of a few millimeters per year using InSAR (Shimotsuma et al. 2026). InSAR is therefore a potentially valuable tool for detecting interseismic displacements associated with plate coupling in regions where dense GNSS

observations are not available. Nevertheless, attempts to estimate plate coupling distributions from InSAR-derived crustal deformation remain limited (Jolivet et al. 2020; Sobouti et al. 2025). This is probably because deep interplate slip produces long-wavelength surface deformation, whose spatial pattern can be constrained by a dense GNSS network. Consequently, the applicability of InSAR to deep interplate slip has remained unclear.

Along the Nankai subduction zone, the Philippine Sea Plate (PH) subducts beneath the Amur Plate (AM) in southwest Japan (Heki et al. 1999) (Fig. 1), and the plate interface between them exhibits various slip behaviors. The estimated coupled regions are mainly distributed at depths shallower than 25 km (Yokota et al. 2016) (Fig. 1b). Seismic slow earthquakes are distributed mainly downdip of the strongly coupled region (Kano et al. 2018) (Fig. 1b). Short-term and long-term slow slip events (S-SSEs and L-SSEs) have been detected mainly by geodetic observations in the transition region between the strongly coupled region and the deeper seismic slow earthquake zone (Ochi 2015; Yabe et al. 2023). Yokota et al. (2026) revealed temporal changes in plate coupling, particularly along the shallow portion of the Nankai subduction zone, using onshore and offshore GNSS observations.

Southwest Japan has dense GNSS and SAR observations, providing a suitable setting for examining the capabilities and limitations of InSAR for estimating plate coupling. Some studies have suggested that incorporating InSAR observations improves the spatial resolution of interplate coupling estimates (Kinoshita and Furuta 2024; Maubant et al. 2023). Shimotsuma et al. (2026) used InSAR observations to investigate plate coupling along the Nankai subduction zone, although they did not consider temporal changes in the plate coupling. In this study, we use both GNSS and InSAR observations from 2014 to 2025 to investigate spatiotemporal changes in the coupling state along the Nankai subduction zone around Shikoku, southwest Japan. InSAR time-series analysis indicates a decrease in the slip deficit rate beneath central Shikoku after 2019, consistent with GNSS observations (Ozawa et al. 2024). We also evaluate the capabilities and limitations of InSAR for constraining deep plate coupling by examining the data fit, estimation uncertainties, and spatial resolution of slip deficit distributions estimated from GNSS, InSAR, and GNSS-InSAR joint inversions.

2. Data and Methods

To detect spatiotemporal changes in the plate coupling state along the Nankai subduction zone, we first estimated GNSS and InSAR displacement velocities around Shikoku for three periods: (i) September 2014 to September 2018, (ii) October 2018 to August 2019, and (iii) September 2019 to March 2025. Period (ii) corresponds to the Bungo Channel L-SSE, whereas period (iii) includes the central Shikoku L-SSE (Ozawa et al. 2024). We then estimated the slip deficit rate distributions along the plate interface for each period through kinematic fault slip inversions using GNSS and InSAR velocity fields.

2.1 GNSS processing

We estimated displacement velocities at the onshore and offshore GNSS stations. For onshore observations, we used the daily coordinates from the GNSS Earth Observation Network System (GEONET; F5.1 analysis strategy) provided by the Geospatial Information Authority of Japan (GSI) (GSI 2026). For offshore observations, we used the coordinate time series obtained from the GNSS-Acoustic ranging (GNSS-A) technique (Yokota et al. 2018) and provided by the Japan Coast Guard (JCG). To extract the displacement velocities caused by the Nankai plate coupling, we corrected the GNSS displacement data for the postseismic displacements of the 2011 Tohoku-oki earthquake (Tobita 2016) and coseismic displacements of the 2016 Kumamoto, 2024 Noto, and 2024 Hyuga nada earthquakes (GSI 2024; Suito et al. 2024; Yarai et al. 2016). We then estimated linear trends (i.e., velocities) for each period. Further details about the GNSS processing are described in Additional file 1: Text S1.

2.2 InSAR processing

We used the Advanced Land Observing Satellite 2 (ALOS-2)/Phased Array-type L-band Synthetic Aperture Radar 2 (PALSAR-2) stripmap mode data acquired from 14 observation frames covering the entire Shikoku region (Additional file 1: Figure S1). We processed the SAR data using GAMMA software. We first concatenated adjacent frames acquired with the same path and off-nadir angle. We refer to the concatenated descending frames as Des-WS, Des-CS, and Des-ES, and the concatenated ascending frames as Asc-WS, Asc-CS, and Asc-ES, where WS, CS, and ES indicate the observation areas of western, central, and eastern Shikoku, respectively (Fig. 1b). We summarize information on the ALOS-2 data in Additional file 1: Table S1. We multilooked all Single Look Complex images to be approximately 100 m pixel spacings in both range and azimuth directions to improve the signal-to-noise ratio. We generated interferograms for all possible pairs in each frame (Additional file 1: Figure S2) with corrections described below. We corrected orbital and topographic fringes using ALOS-2 precise orbit information and the 30 m resolution digital elevation model of the Shuttle Radar Topography Mission (Farr et al. 2007). We applied a spectral filter (Goldstein and Werner 1998), and we then performed two-dimensional phase unwrapping based on the minimum-flow algorithm (Costantini 1998). We corrected ionospheric phase advance using the Split Spectrum Method (Wegmüller et al. 2018) and neutral atmospheric delay using GNSS atmospheric products (Kinoshita 2022). We also corrected phase changes due to the solid earth tide using the PySolid module (Yunjun et al. 2022; Milbert 2018). The coseismic and postseismic effects described in subsection 2.1 were also corrected as done in the GNSS processing. We subsequently estimated LOS velocity fields for the three periods using a small baseline subset-based time-series analysis approach (Berardino et al. 2002). Further details of the InSAR processing are described in Additional file 1: Text S2.

2.3 Kinematic fault slip inversion

We estimated the slip deficit rate distributions along the Nankai subduction zone using kinematic least-squares inversions of GNSS and InSAR velocity fields. Additional file 1: Figure S1 shows the GNSS and InSAR data used in the inversions. We distributed 406 triangular subfaults on a plate interface model (Iwasaki et al. 2015; Lindquist et al. 2004) at depths of 0–40 km (Additional file 1: Figure S1), considering that stable sliding is thought to occur at depths greater than 40 km (Obara and Kato 2016). The slip

direction was assumed parallel to the AM-PH convergence direction (DeMets et al. 2010). We calculated the surface displacements due to subfault slip using a triangular dislocation model in a homogeneous elastic half-space (Lindsey 2024; Nikkhoo and Walter 2015). For each period, we performed three inversion cases for comparison: GNSS-only, InSAR-only, and GNSS-InSAR joint inversions. For all cases, we applied a spatial smoothing constraint to the slip deficit rate distributions (Maerten et al. 2005). Here, we applied a non-uniform smoothing constraint based on the resolution matrix of the model parameters (Ader et al. 2012), which allows the smoothing strength to vary according to the local resolving power of the observations. The smoothing strength and the relative weight between the GNSS and InSAR data were optimized based on the Akaike Bayesian Information Criterion (Funning et al. 2014). Further details of the kinematic fault slip inversion are provided in Additional file 1: Text S3.

3. Results

3.1 Observed velocity fields

Figure 2 shows the observed GNSS and InSAR velocities in periods (i) and (iii) together with the velocity differences between the two periods. All velocities are expressed in an AM-fixed reference frame. The velocity profiles along the trough-normal lines (A–N in Fig. 2) are shown in Additional file 1: Figures S3–S6. The root mean square errors (RMSEs) between InSAR and GNSS velocities in the LOS direction for each frame (Additional file 1: Table S2) are less than 2.5 mm/year in period (iii), showing good agreement. In period (i), the RMSEs for the ascending frames are relatively large (> 4.0 mm/year). The InSAR velocities in period (ii) appear noisy (Additional file 1: Figure S7) because only a few SAR acquisitions were available during period (ii). Hereafter, we focus on the results for periods (i) and (iii).

The GNSS horizontal velocities in Shikoku are roughly parallel to the AM-PH convergence direction and decrease with increasing distance from the Nankai Trough (Fig. 2, Additional file 1: Figure S3). The GNSS vertical velocities show downward motion in the offshore region and around Cape Ashizuri and Cape Muroto, gradually changing to upward motion in Shikoku, reaching a positive maximum within Shikoku, and then decreasing further from the trough (Fig. 2, Additional file 1: Figure S4). In general, the InSAR velocities are largest along the southern coast of Shikoku and gradually decrease northward (Fig. 2, Additional file 1: Figures S5 and S6). These spatially long-wavelength GNSS and InSAR velocity patterns are consistent with the theoretical elastic deformation owing to plate coupling. The velocity fields show no apparent discontinuities along the inland faults, implying that these faults do not exhibit creep at shallow depths in Shikoku.

Comparing periods (i) and (iii), we find that the GNSS vertical velocity differences are negative at many stations across the study area while positive velocity changes of a few mm/year exist around south-central Shikoku (Fig. 2c). In contrast, horizontal velocities increase in the southeastward direction over a wider area from south-central to northwestern Shikoku. Some stations (e.g., “950436” shown in Additional file 1: Figure S1) show anomalous velocity changes that may reflect non-tectonic phenomena such as landslides, because their velocity changes deviate from those of the surrounding GNSS stations.

The GNSS-A stations show larger velocity changes than the GEONET stations; however, these changes are associated with large observation uncertainties (Additional file 1: Figure S8). The InSAR velocity changes may include remaining topography-correlated noise. Nevertheless, both the descending and ascending frames show negative LOS velocity changes over south-central Shikoku (Figs. 2f and 2i), implying that upward velocities increase. Considering that these velocity changes in south-central Shikoku extend over several tens of kilometers, they are likely to reflect coupling rate variations at deep deformation source areas.

3.2 Spatiotemporal change in slip deficits along the Nankai subduction zone

We show three cases of slip deficit distributions along the Nankai subduction zone estimated using only GNSS (GEONET and GNSS-A) velocities (hereafter called “GNSS model”), only InSAR velocities (hereafter called “InSAR model”), and both GNSS and InSAR velocities (hereafter called “joint model”) for each period in Fig. 3. Slip deficit rate distributions shown in Fig. 3 are estimated with an assumption that slip deficit rates are close to zero along the entire boundary of the fault model domain. For periods (i) and (iii), we estimate large slip deficit rates off Shikoku and in the Kii Peninsula, where large coseismic slips of the 1944 Tonankai (M_w 8.1) and 1946 Nankai (M_w 8.3) megathrust earthquakes have been estimated in previous studies (Sherrill and Johnson 2021).

Figures 4 and 5 show the observed, calculated, and residual velocities for the joint models in periods (i) and (iii), respectively. We show those for the GNSS and InSAR models in Additional file 1: Figures S9–S12. Overall, calculated velocities reproduce the large-scale spatial patterns of the observed velocities. However, we recognize some systematic and/or localized residual velocities. In both periods, the GNSS residuals show eastward velocities in the southern Chugoku region (E133°– E134.5°) and westward and upward velocities in the Kii Peninsula (Figs. 4c and 5c). The GNSS-A stations show larger residual velocities than the GEONET stations, which may reflect their larger observation uncertainties associated with sparse temporal sampling. The InSAR residual velocities show topography-correlated spatial patterns, particularly in period (i), suggesting the presence of remaining topography-correlated noise such as residual neutral atmospheric delays. Consistently, the root mean square (RMS) values of the InSAR residual velocities are larger in period (i) than in period (iii) (Table 1), which partly originate from larger observation noise in period (i). Thus, for the period (i), the relative weight for InSAR data with respect to GNSS data becomes small in the inversion, which makes the joint model (Fig. 3g) similar to the GNSS model (Fig. 3a).

Table 1
Root mean square (RMS) values [mm/year] of residual velocities for each period and model.

Period	**Period (i)**			**Period (iii)**		
Model	GNSS (Fig. S9)	InSAR (Fig. S11)	Joint (Fig. 4)	GNSS (Fig. S10)	InSAR (Fig. S12)	Joint (Fig. 5)
GEONET eastward	1.77	-	1.78	1.55	-	1.67
GEONET northward	1.12	-	1.14	0.79	-	0.85
GEONET upward	2.59	-	2.76	2.10	-	2.17
GNSS-A eastward	7.52	-	7.49	9.22	-	9.24
GNSS-A northward	8.56	-	8.67	6.25	-	6.38
GNSS-A upward	13.5	-	13.5	9.45	-	8.97
Des-WS	-	2.19	2.30	-	1.15	1.64
Des-CS	-	2.41	2.46	-	1.44	1.64
Des-ES	-	1.96	2.07	-	1.28	1.27
Asc-WS	-	3.95	3.95	-	1.91	1.87
Asc-CS	-	6.15	6.38	-	1.27	1.37
Asc-ES	-	4.61	4.28	-	1.83	1.40

We emphasize that both the GNSS- and InSAR-based models show broadly similar spatial patterns of slip deficit rates beneath Shikoku (Fig. 3), where GNSS and InSAR observations are densely distributed. Both models show a decrease in slip deficit rates beneath central Shikoku in period (iii) compared to period (i) (Figs. 3c and f). The maximum decrease in slip deficit rate beneath central Shikoku is 39 mm/year in the GNSS-based model and 41 mm/year in the InSAR-based model. These decreases in central Shikoku are larger than estimation uncertainties, defined here as standard errors of the estimated slip deficit rates, in both periods (i) and (iii) (Fig. 6). The standard errors are calculated as the square roots of the diagonal elements of the model-parameter covariance matrix, as defined in equation (S32) in Additional file 1: Text S3. The InSAR model shows an increase in slip deficit rate around northwestern Shikoku, while the GNSS and joint models do not. Whether this increase reflects an actual change in plate coupling is doubtful because it is not reproduced by the GNSS or joint models. Although such a discrepancy exists, all three models consistently show a significant decrease in slip deficit rate beneath central Shikoku. This agreement between the GNSS- and InSAR-based models supports the robustness of the estimated slip deficit decrease beneath central Shikoku. Additional file 1: Figure S13 shows the theoretical displacement velocity changes calculated from the slip deficit rate changes in the joint model between periods (i) and (iii) (Fig. 3i). For this calculation, we used only the subfaults where the magnitude of change exceeded the standard errors of the estimated slip deficit rates in both periods (i)

and (iii). These simulated displacement velocity patterns are roughly consistent with the observed GNSS and InSAR velocity changes (Fig. 2). The simulated displacement velocity changes show upward velocities in south-central Shikoku and southeastward velocities extending from south-central to northwestern Shikoku (Additional file 1: Figure S13).

4. Discussions

4.1 Decrease in slip deficit around central Shikoku after 2019

All the GNSS, InSAR, and joint models suggest that slip deficit rates decreased beneath central Shikoku in period (iii) compared to period (i). This decrease in slip deficits spatially corresponds to the central Shikoku L-SSE, which began in 2019, as reported by Ozawa et al. (2024). Ozawa et al. (2024) detected transient GNSS displacements that began in 2019, after removing linear trends estimated from the reference period (January–December 2017), and they estimated a fault slip model to explain these displacements. Therefore, their fault slip model represented the slip since 2019 relative to the selected reference period, and they interpreted this relative slip as an L-SSE. However, we do not interpret this as an L-SSE, following the concept proposed by Ochi and Kato (2013). Ochi and Kato (2013) proposed a no-coupling state as a reference for interpreting interplate coupling and aseismic slip. In this framework, an SSE corresponds to the updip slip of the hanging-wall side, and the estimated slip amount of the SSE does not depend on the choice of reference period. Our estimated slip deficit rates do not show significantly negative values around central Shikoku during period (iii) (Figs. 3b, e, and h). Therefore, we interpret this slip deficit decrease beneath central Shikoku after 2019 as a temporal weakening of plate coupling rather than an L-SSE.

Note that our estimated slip deficit rates represent temporal averages over each period and therefore do not resolve short-term variations. Ozawa et al. (2023, 2024) estimated that aseismic slip beneath central Shikoku accelerated especially around 2019 and 2022 using daily GNSS data. The multi-year decrease in slip deficit identified in this study probably includes shorter-term perturbations superimposed on the longer-term coupling weakening.

Another coupling change was reported beneath central Shikoku from 1977 to 1980. Kobayashi (2012) detected unsteady uplift of < 4–5 cm around Kochi city, south-central Shikoku, from 1977 to 1980 using leveling and sea-level data. The corresponding fault model estimated by Kobayashi (2012) was located slightly west of the coupling change since 2019. Because the spatiotemporal coverage of geodetic observations was limited, it is still difficult to determine the regularity and recurrence intervals of such coupling changes beneath central Shikoku. Nevertheless, the available past and current observations suggest that the plate interface beneath central Shikoku has undergone long-term changes in the coupling state during the interseismic period.

The estimated slip deficit decrease beneath central Shikoku is centered at a depth of approximately 25 km (Fig. 3). This region is located between the seismogenic zone and the deep slow earthquake zone (Fig. 1b) and is slightly above the continental Mohorovičić discontinuity (Yoshioka and Murakami 2007). The temperature at this location is estimated to be approximately 400°C (Yoshioka and Murakami 2007). Matsubara et al. (2022) estimated relatively high V_p/V_s ratios beneath central Shikoku at a depth of 30 km, which may be related to dehydration of the PH (Gao and Wang 2017). These characteristics may indicate that a frictional transition from velocity-weakening to velocity-strengthening and a low effective normal stress exist beneath central Shikoku. Numerical simulations have shown that such conditions promote long-term aseismic slip (Liu and Rice 2005; Matsuzawa et al. 2013). These factors may also contribute to the long-term changes in plate coupling.

4.2 Benefits and limitations of InSAR application for estimating plate coupling

Our results show that slip deficit distributions estimated from GNSS and those estimated from InSAR are similar to each other in the inland region, suggesting that InSAR potentially constrains the plate coupling state independently of GNSS. This similarity in the inland region can be explained by the sensitivity of InSAR observations to vertical displacements. Aoki and Scholz (2003) suggested that dip slips in deeper regions of the plate interface significantly affect the spatial pattern of vertical displacements in inland regions. In contrast, horizontal displacements in the Nankai region are dominated by coupling beneath the offshore region at depths shallower than 25 km (Tabei et al. 2007). InSAR LOS observations used in this study are more sensitive to vertical displacement than to horizontal displacement. Therefore, InSAR observations used in this study are suitable for detecting changes in plate coupling beneath the inland region. Our results suggest that InSAR has the potential to estimate plate coupling states in subduction zones where GNSS observations are limited.

We examined the sensitivity of the estimated slip deficit rates to the boundary conditions on the fault model domain. We also estimated slip deficit rate distributions by assuming a free-slip boundary condition (Additional file 1: Figure S14). Comparing the estimates obtained with zero-slip (Fig. 3) and free-slip (Additional file 1: Figure S14) boundary conditions, the estimated slip deficit rates along the Nankai Trough are highly sensitive to the boundary conditions. In contrast, the estimated slip deficit rates beneath Shikoku are less sensitive to the boundary conditions and are thus well constrained by the observed velocities.

A comparison of the GNSS and joint models shows that the addition of InSAR velocities slightly improves the spatial resolution of the estimated slip deficit distributions beneath inland regions when InSAR velocities are accurate to some extent, as in period (iii) (Fig. 7, Additional file 1: Figure S15). In period (i), InSAR velocities are noisier than those in period (iii), and InSAR velocities improve the resolution less than in period (iii). Another reason why InSAR did not drastically improve the resolution is that we imposed a smoothing constraint in the inversion analysis. In addition, Japan has spatially dense onshore GNSS observations; the spatial separation between GEONET stations is approximately 20 km.

Because the long-wavelength displacements associated with deep plate coupling can already be captured by such a dense GNSS network, adding InSAR does not drastically improve the spatial resolution of the estimated plate coupling distribution. Nevertheless, the InSAR model reproduces the broad-scale spatial pattern of plate coupling changes beneath inland Shikoku, which demonstrates that InSAR provides independent constraints on such long-wavelength coupling changes beneath inland regions.

The above results indicate that detectability of changes in plate coupling by InSAR depends on their location and spatial scale. The detectability also depends on the magnitude of the coupling changes relative to the observation uncertainty. Physics-based simulations have suggested that the coupled region on the plate interface narrows in the dip direction during interseismic periods (Bruhat and Segall 2017; Hori et al. 2004). For example, a crack model reported by Bruhat and Segall (2017) predicted that the locking depth would migrate updip at a speed of 30–120 m/year, producing surface accelerations on the order of 10^{-2} mm/year^2. It is impossible to detect such a theoretical migration considering the accuracy and the resolving power of GNSS and InSAR observations. On the other hand, GNSS observations detected surface displacement accelerations of a few mm/year² in south-central Tohoku before the 2011 Tohoku-oki earthquake (Mavrommatis et al. 2014), which were attributed to an increase in interplate slip rate downdip of the seismogenic zone and/or to updip migration of deep aseismic slip. The observed accelerations in surface displacement rate were more than one order of magnitude larger than those predicted by the crack model of Bruhat and Segall (2017). Such surface displacement acceleration is practically detectable by InSAR time-series analysis. Our results show that InSAR velocities contain larger errors than interseismic signal when the number of SAR acquisitions is limited, as indicated by the residual velocity fields (Figs. 4 and 5). Increasing the number of SAR data reduces the temporally independent noise during the time-series analysis and improves the detectability of smaller changes in plate coupling.

The detectability of changes in plate coupling also depends on their temporal scale relative to the temporal sampling of SAR observations. Although ALOS-2 data used in this study have long observation intervals (several months), other satellites with shorter observation intervals help detect shorter events. For example, a single Sentinel-1 satellite has a 12-day repeat cycle, which is reduced to six days when two satellites operate as a constellation. Such high-frequency SAR observations from Sentinel-1 allowed the detection of S-SSEs (Kinoshita and Furuta 2024). New satellites, such as ALOS-4 and the National Aeronautics and Space Administration-Indian Space Research Organization Synthetic Aperture Radar, also have relatively short observation intervals (less than two weeks). These improvements in the frequency of SAR satellite observations will contribute to future detection of unknown coupling changes in subduction zones.

5. Conclusion

Using GNSS and InSAR observations from 2014 to 2025, we estimated spatiotemporal changes in the slip deficit distribution along the Nankai subduction zone. All three case models (GNSS, InSAR, and joint

models) show that the slip deficit rates beneath central Shikoku decreased after 2019 relative to 2014–2018. The spatial pattern of this decrease inferred from the InSAR model is roughly consistent with that from the GNSS model, and spatially corresponds to the L-SSE reported by Ozawa et al. (2024). We interpret this slip deficit decrease as a temporal weakening of plate coupling rather than an L-SSE. This is because the estimated slip deficits beneath central Shikoku do not show significantly negative values after 2019. We emphasize that GNSS and InSAR independently infer broadly similar spatial patterns of the slip deficit change beneath the Shikoku region. This consistency can be attributed to the high sensitivity of InSAR LOS observations to vertical displacement, whose spatial pattern in inland regions is dominated by dip slip on the downdip portion of the plate interface. This suggests that InSAR observations provide valuable constraints on interplate coupling changes, particularly in inland regions where dense GNSS observations are not available.

Abbreviations

ALOS-2
Advanced Land Observing Satellite 2
AM
Amur plate
GEONET
GNSS Earth Observation Network System
GNSS
Global Navigation Satellite System
GNSS-A
GNSS-Acoustic ranging
GSI
Geospatial Information Authority of Japan
InSAR
Interferometric Synthetic Aperture Radar
JCG
Japan Coast Guard
L-SSE
long-term slow slip event
LOS
line-of-sight
PALSAR-2
Phased Array-type L-band Synthetic Aperture Radar 2
PH
Philippine Sea plate
RMSE
root mean square error

RMS
root mean square
SAR
synthetic aperture radar
SSE
slow slip event
S-SSE
short-term slow slip event

Declarations

Ethics approval and consent to participate

Not applicable.

Consent for publication

Not applicable

Availability of data and materials

ALOS-2/PALSAR-2 data were shared with the PALSAR Interferometry Consortium to Study our Evolving Land surface (PIXEL) group and were provided by the Japan Aerospace Exploration Agency (JAXA) under a cooperative research contract with PIXEL. The ownership of PALSAR-2 data belongs to JAXA. The Shuttle Radar Topography Mission (SRTM) digital elevation model (DEM) (Farr et al. 2007) is available on the U.S. Geological Survey (USGS) homepage (https://earthexplorer.usgs.gov/). Five-minute GNSS delay data were downloaded from the homepage of the Nevada Geodetic Laboratory at the University of Nevada (https://geodesy.unr.edu/gps_timeseries/IGS20/). The GEONET daily coordinates (GSI 2026) are available on the GSI homepage (https://www.gsi.go.jp/denshi/GSI_GNSS_2026_001.html) with registration, whereas the GNSS-A coordinates (Yokota et al. 2018) are available on the JCG homepage (https://www1.kaiho.mlit.go.jp/chikaku/kaitei/sgs/gnss-a_timeseries.html). The plate model (Iwasaki et al. 2015) is available on the website of Dr. Iwasaki (https://wwweic.eri.u-tokyo.ac.jp/evrrss/database/PLATEmodel/). The slip deficit rate distribution estimated by Yokota et al. (2016) (shown in Figure 1b in this paper) is available in Supplementary Table 2 of Yokota et al. (2016). You can access the “Active fault database of Japan (National Institute of Advanced Industrial Science and Technology 2026)” from https://gbank.gsj.jp/activefault/index_e.html, and “Slow Earthquake database (Kano et al. 2018)” from http://www-solid.eps.s.u-tokyo.ac.jp/~sloweq/. The tdcalc software to calculate displacements due to triangular dislocations (Nikkhoo and Walter 2015) was developed by Lindsey (2024) and is available at https://doi.org/10.5281/zenodo.12802953. We provide our results, including GNSS and InSAR velocities and estimated slip deficit rates, on Zenodo. For peer review, the

dataset is available through a private Zenodo link provided in the separately uploaded text file “zenodo_URL.txt”.

Competing interests

The authors declare that they have no competing interests.

Funding

This study was financially supported by the JST SPRING (Grant No. JPMJSP2124); ERI, the University of Tokyo (ERI Joint Usage Research Program 2024-B-02); JSPS KAKENHI (Grant No. 21H04505); MEXT KAKENHI (Grant No. 21H05203); Young Researcher Training Program, Graduate School of Systems and Information Engineering, University of Tsukuba; and cooperative research with ME-Lab Japan and LTS.

Authors’ contributions

K.S. and S.Y. conceived the original idea, which was elaborated on by Y.K. and T.O. InSAR processing was conducted mainly by K.S., with supervision by Y.K. Y.K. developed the neutral atmospheric correction program. GNSS processing and kinematic fault slip inversion were conducted by K.S., with comments from Y.K., S.Y. and T.O. K.S. prepared the figures, tables and manuscript, which were modified by Y.K., S.Y. and T.O.

Acknowledgements

This study was financially supported by the JST SPRING (Grant No. JPMJSP2124); ERI, the University of Tokyo (ERI Joint Usage Research Program 2024-B-02); JSPS KAKENHI (Grant No. 21H04505); MEXT KAKENHI (Grant No. 21H05203); Young Researcher Training Program, Graduate School of Systems and Information Engineering, University of Tsukuba; and cooperative research with ME-Lab Japan and LTS. In InSAR processing, we used ALOS-2/PALSAR-2 data shared among the PIXEL group and provided by JAXA under a cooperative research contract with PIXEL. The ownership of PALSAR-2 data belongs to JAXA. We used the SRTM DEM (Farr et al. 2007) provided by the USGS. Five-minute GNSS atmospheric products were processed and provided by the Nevada Geodetic Laboratory at the University of Nevada. In the GNSS processing, we used GEONET data “F5.1 analysis strategy (GSI 2026)” provided by the GSI and GNSS-A data (Yokota et al. 2018) provided by the JCG. In the kinematic inversion, we used the dislocation model “tdcalc” (Lindsey 2024; Nikkhoo and Walter 2015). The plate model by Iwasaki et al. (2015) was constructed from topography and bathymetry data from the GSI (250-m digital map), Japan Oceanographic Data Center (500 m mesh bathymetry data, J-EGG500, http://www.jodc.go.jp/jodcweb/JDOSS/infoJEGG_j.html), and the Geographic Information Network of Alaska, University of Alaska (Lindquist et al. 2004). We used the “Active Fault Database of Japan

(National Institute of Advanced Industrial Science and Technology 2026)" and the "Slow Earthquake Database (Kano et al. 2018)" for mapping.

References

1. Ader T, Avouac JP, Liu-Zeng J et al (2012) Convergence rate across the Nepal Himalaya and interseismic coupling on the Main Himalayan Thrust: implications for seismic hazard. J Geophys Res Solid Earth 117:B04403. 10.1029/2011JB009071
2. Aoki Y, Scholz CH (2003) Interseismic deformation at the Nankai subduction zone and the Median Tectonic Line, southwest Japan. J Geophys Res Solid Earth 108(B10):2470. 10.1029/2003JB002441
3. Berardino P, Fornaro G, Lanari R, Sansosti E (2002) A new algorithm for surface deformation monitoring based on small baseline differential SAR interferograms. IEEE Trans Geosci Remote Sens 40(11):2375–2383. 10.1109/TGRS.2002.803792
4. Bruhat L, Segall P (2017) Deformation rates in northern Cascadia consistent with slow updip propagation of deep interseismic creep. Geophys J Int 211(1):427–449. 10.1093/gji/ggx317
5. Costantini M (1998) A novel phase unwrapping method based on network programming. IEEE Trans Geosci Remote Sens 36(3):813–821. 10.1109/36.673674
6. DeMets C, Gordon RG, Argus DF (2010) Geologically current plate motions. Geophys J Int 181(1):1–80. 10.1111/j.1365-246X.2009.04491.x
7. Farr TG, Rosen PA, Caro E et al (2007) The Shuttle Radar Topography Mission. Rev Geophys 45(2):RG2004. 10.1029/2005RG000183
8. Funning GJ, Fukahata Y, Yagi Y, Parsons B (2014) A method for the joint inversion of geodetic and seismic waveform data using ABIC: application to the 1997 Manyi, Tibet, earthquake. Geophys J Int 196(3):1564–1579. 10.1093/gji/ggt406
9. Gao X, Wang K (2017) Rheological separation of the megathrust seismogenic zone and episodic tremor and slip. Nature 543(7645):416–419. 10.1038/nature21389
10. Geospatial Information Authority of Japan (2024) Fault model for the 2024 Hyūga-nada earthquake (in Japanese). https://www.gsi.go.jp/common/000260639.pdf. Accessed 24 Sep 2026
11. Geospatial Information Authority of Japan (2026) GEONET products (F5.1 analysis strategy). https://www.gsi.go.jp/denshi/GSI_GNSS_2026_001.html. Accessed 23 Sep 2026
12. Goldstein RM, Werner CL (1998) Radar interferogram filtering for geophysical applications. Geophys Res Lett 25(21):4035–4038. 10.1029/1998GL900033
13. Heki K, Miyazaki SI, Takahashi H et al (1999) The Amurian Plate motion and current plate kinematics in eastern Asia. J Geophys Res Solid Earth 104(B12):29147–29155. 10.1029/1999JB900295
14. Hori T, Kato N, Hirahara K, Baba T, Kaneda Y (2004) A numerical simulation of earthquake cycles along the Nankai Trough in southwest Japan: lateral variation in frictional property due to the slab

geometry controls the nucleation position. Earth Planet Sci Lett 228(3–4):215–226. 10.1016/j.epsl.2004.09.033

15. Iwasaki T, Sato H, Shinohara M, Ishiyama T, Hashima A (2015) Fundamental structure model of island arcs and subducted plates in and around Japan. Paper presented at the 2015 AGU Fall Meeting, San Francisco, CA, 14–18 Dec 2015, abstract T31B-2878
16. Jolivet R, Simons M, Duputel Z, Olive JA, Bhat HS, Bletery Q (2020) Interseismic loading of subduction megathrust drives long-term uplift in northern Chile. Geophys Res Lett 47(8):e2019GL085377. 10.1029/2019GL085377
17. Kano M, Aso N, Matsuzawa T et al (2018) Development of a slow earthquake database. Seismol Res Lett 89(4):1566–1575. 10.1785/0220180021
18. Kinoshita Y (2022) Development of InSAR neutral atmospheric delay correction model by use of GNSS ZTD and its horizontal gradient. IEEE Trans Geosci Remote Sens 60:5231414. 10.1109/TGRS.2022.3188988
19. Kinoshita Y, Furuta R (2024) Slow slip event displacement on 2018 offshore Boso Peninsula detected by Sentinel-1 InSAR time-series analysis with numerical weather model assistance. Geophys J Int 237(1):75–89. 10.1093/gji/ggae028
20. Kobayashi A (2012) Long-term slow slip event around Kochi City from 1977 to 1980 (in Japanese). Zisin 64(2):63–73. 10.4294/zisin.64.63
21. Lindquist KG, Engle K, Stahlke D, Price E (2004) Global topography and bathymetry grid improves research efforts. Eos Trans Am Geophys Union 85(19):186. 10.1029/2004EO190003
22. Lindsey EO (2024) tdcalc version 1.0. Zenodo. https://doi.org/10.5281/zenodo.12802953
23. Liu Y, Rice JR (2005) Aseismic slip transients emerge spontaneously in three-dimensional rate and state modeling of subduction earthquake sequences. J Geophys Res Solid Earth 110(B8):B08307. 10.1029/2004JB003424
24. Maerten F, Resor P, Pollard D, Maerten L (2005) Inverting for slip on three-dimensional fault surfaces using angular dislocations. Bull Seismol Soc Am 95(5):1654–1665. 10.1785/0120030181
25. Matsubara M, Ishiyama T, No T et al (2022) Seismic velocity structure along the Sea of Japan with large events derived from seismic tomography for whole Japanese Islands including reflection survey data and NIED MOWLAS Hi-net and S-net data. Earth Planet Space 74:171. 10.1186/s40623-022-01724-0
26. Matsuzawa T, Shibazaki B, Obara K, Hirose H (2013) Comprehensive model of short- and long-term slow slip events in the Shikoku region of Japan, incorporating a realistic plate configuration. Geophys Res Lett 40(19):5125–5130. 10.1002/grl.51006
27. Maubant L, Frank WB, Wallace LM, Williams CA, Hamling I (2023) Imaging the spatiotemporal evolution of plate coupling with interferometric radar (InSAR) in the Hikurangi subduction zone. Geophys Res Lett 50(19):e2023GL105388. 10.1029/2023GL105388
28. Mavrommatis AP, Segall P, Johnson KM (2014) A decadal-scale deformation transient prior to the 2011 Mw 9.0 Tohoku-oki earthquake. Geophys Res Lett 41:4486–4494. 10.1002/2014GL060139

29. Mavrommatis AP, Segall P, Uchida N, Johnson KM (2015) Long-term acceleration of aseismic slip preceding the Mw 9 Tohoku-oki earthquake: constraints from repeating earthquakes. Geophys Res Lett 42:9717–9725. 10.1002/2015GL066069
30. Milbert D (2018) solid: Solid Earth Tide. http://geodesyworld.github.io/SOFTS/solid.htm. Accessed 7 Aug 2026
31. National Institute of Advanced Industrial Science and Technology (2026) Active Fault Database of Japan, 23 June 2026 version. https://gbank.gsj.jp/activefault/ Accessed 23 Sep 2026
32. Nikkhoo M, Walter TR (2015) Triangular dislocation: an analytical, artefact-free solution. Geophys J Int 201(2):1119–1141. 10.1093/gji/ggv035
33. Nishimura T, Yokota Y, Tadokoro K, Ochi T (2018) Strain partitioning and interplate coupling along the northern margin of the Philippine Sea plate, estimated from Global Navigation Satellite System and Global Positioning System-Acoustic data. Geosphere 14(2):535–551. 10.1130/GES01529.1
34. Obara K, Kato A (2016) Connecting slow earthquakes to huge earthquakes. Science 353(6296):253–257. 10.1126/science.aaf1512
35. Ochi T, Kato T (2013) Depth extent of the long-term slow slip event in the Tokai district, central Japan: a new insight. J Geophys Res Solid Earth 118(9):4847–4860. 10.1002/jgrb.50355
36. Ochi T (2015) Temporal change in plate coupling and long-term slow slip events in southwestern Japan. Earth Planet Sci Lett 431:8–14. 10.1016/j.epsl.2015.09.012
37. Ozawa S, Munekane H, Suito H (2023) Detection of long- and short-term slow slip events using a network inversion filter and dense global navigation satellite system network in Shikoku, Japan. J Geophys Res Solid Earth 128. 10.1029/2023JB026557. :e2023JB026557
38. Ozawa S, Muneakane H, Suito H (2024) Time-dependent modeling of slow-slip events along the Nankai Trough subduction zone, Japan, within the 2018–2023 period. Earth Planet Space 76:23. 10.1186/s40623-024-01970-4
39. Plata-Martinez R, Iinuma T, Tomita F, Nakamura Y, Nishimura T, Hori T (2024) Revisiting slip deficit rates and its insights into large and slow earthquakes at the Nankai subduction zone. J Geophys Res Solid Earth 129(12). e2023JB027942
40. Segall P, Bradley AM (2012) Slow-slip evolves into megathrust earthquakes in 2D numerical simulations. Geophys Res Lett 39(18):L18308. 10.1029/2012GL052811
41. Sherrill EM, Johnson KM (2021) New insights into the slip budget at Nankai: an iterative approach to estimate coseismic slip and afterslip. J Geophys Res Solid Earth 126(2):e2020JB020833. 10.1029/2020JB020833
42. Shimotsuma K, Kinoshita Y, Yabe S, Ochi T (2026) Estimation of the fault geometry of the Median Tectonic Line (MTL) in eastern Shikoku, southwestern Japan, via GNSS and InSAR time series analysis. Earth Planet Space 78:30. 10.1186/s40623-025-02339-x
43. Sobouti A, Samiei Esfahany S, Sharifi MA, Abolghasem AM, Bahroudi A, Friedrich AM (2025) Kinematics of the western Makran subduction zone: insights from InSAR analysis of interseismic coupling. J Geophys Res Solid Earth 130(9). e2025JB031167

44. Suito H, Munekane H, Kuwahara M (2024) Fault model of the 2024 Noto Peninsula earthquake (in Japanese). J Geospatial Inform Auth Japan 138:33–38. 10.57499/JOURNAL_138_05
45. Tabei T, Adachi M, Miyazaki S, Watanabe T, Kato S (2007) Interseismic deformation of the Nankai subduction zone, southwest Japan, inferred from three-dimensional crustal velocity fields. Earth Planet Space 59(10):1073–1082. 10.1186/BF03352050
46. Tobita M (2016) Combined logarithmic and exponential function model for fitting postseismic GNSS time series after 2011 Tohoku-Oki earthquake. Earth Planet Space 68:41. 10.1186/s40623-016-0422-4
47. Wegmüller U, Werner C, Frey O, Magnard C, Strozzi T (2018) Reformulating the split-spectrum method to facilitate the estimation and compensation of the ionospheric phase in SAR interferograms. Procedia Comput Sci 138:318–325. 10.1016/j.procs.2018.10.045
48. Yabe S, Ochi T, Matsumoto N, Itaba S, Kitagawa Y, Matsuzawa T (2023) Eight-year catalog of deep short-term slow slip events at the Nankai trough based on objective detection algorithm using strain and tilt records. Earth Planet Space 75:13. 10.1186/s40623-023-01769-9
49. Yarai H, Kobayashi T, Morishita Y et al (2016) Source fault models of the 2016 Kumamoto Earthquake inverted from crustal deformation (in Japanese). J Geospatial Inform Auth Japan 128:169–176. 10.57499/JOURNAL_128_28
50. Yokota Y, Ishikawa T, Watanabe S, Tashiro T, Asada A (2016) Seafloor geodetic constraints on interplate coupling of the Nankai Trough megathrust zone. Nature 534(7607):374–377. 10.1038/nature17632
51. Yokota Y, Ishikawa T, Watanabe SI (2018) Seafloor crustal deformation data along the subduction zones around Japan obtained by GNSS-A observations. Sci Data 5:180182. 10.1038/sdata.2018.182
52. Yokota Y, Watanabe S, Nagae K, Nakamura Y, Noda A, Ishikawa T (2026) Decadal seafloor geodesy reveals constantly locked areas and temporal changes in the slip deficit rate along the Nankai Trough. Earth Planet Space 78:116. 10.1186/s40623-026-02472-1
53. Yoshioka S, Murakami K (2007) Temperature distribution of the upper surface of the subducted Philippine Sea Plate along the Nankai Trough, southwest Japan, from a three-dimensional subduction model: relation to large interplate and low-frequency earthquakes. Geophys J Int 171(1):302–315. 10.1111/j.1365-246X.2007.03510.x
54. Yunjun Z, Fattahi H, Pi X et al (2022) Range geolocation accuracy of C-/L-band SAR and its implications for operational stack coregistration. IEEE Trans Geosci Remote Sens 60:5227219. 10.1109/TGRS.2022.3168509

Figures

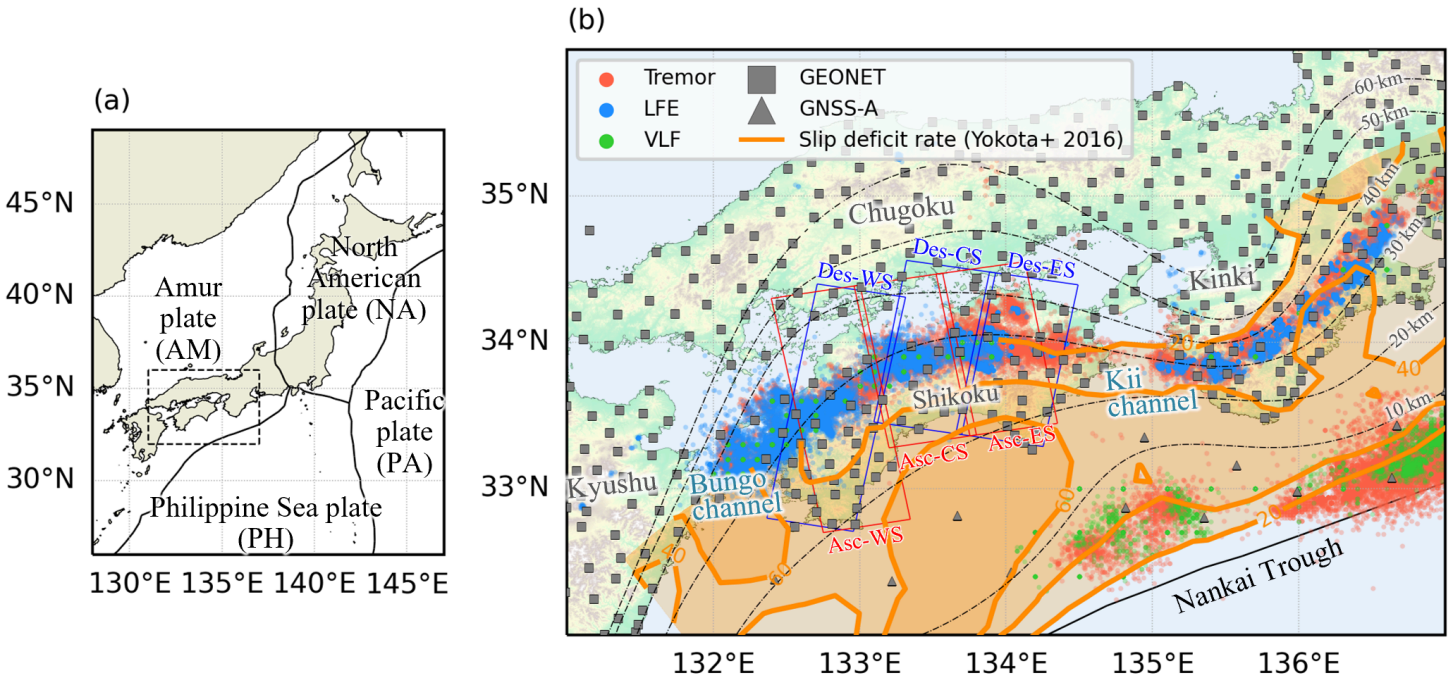


Figure 1

Tectonic setting around the study area. (a) Plate tectonic setting of the Japanese islands. The solid lines indicate plate boundaries. (b) Geographic conditions within the dashed square in (a). Red, blue, and green dots indicate tectonic tremors, low-frequency earthquakes (LFEs), and very-low-frequency earthquakes (VLFEs), respectively, that occurred from September 2014 to December 2023, as compiled from the “Slow Earthquake Database” (Kano et al.). Orange solid lines indicate interseismic slip deficit rates estimated by Yokota et al. () from onshore and offshore Global Navigation Satellite System (GNSS) displacements, with an interval of 20 mm/year. Blue and red rectangles show observation frames of the Advanced Land Observing Satellite 2 (ALOS-2) satellite used in this study. Dash-dotted lines represent depth contours of the plate interface, with an interval of 10 km.

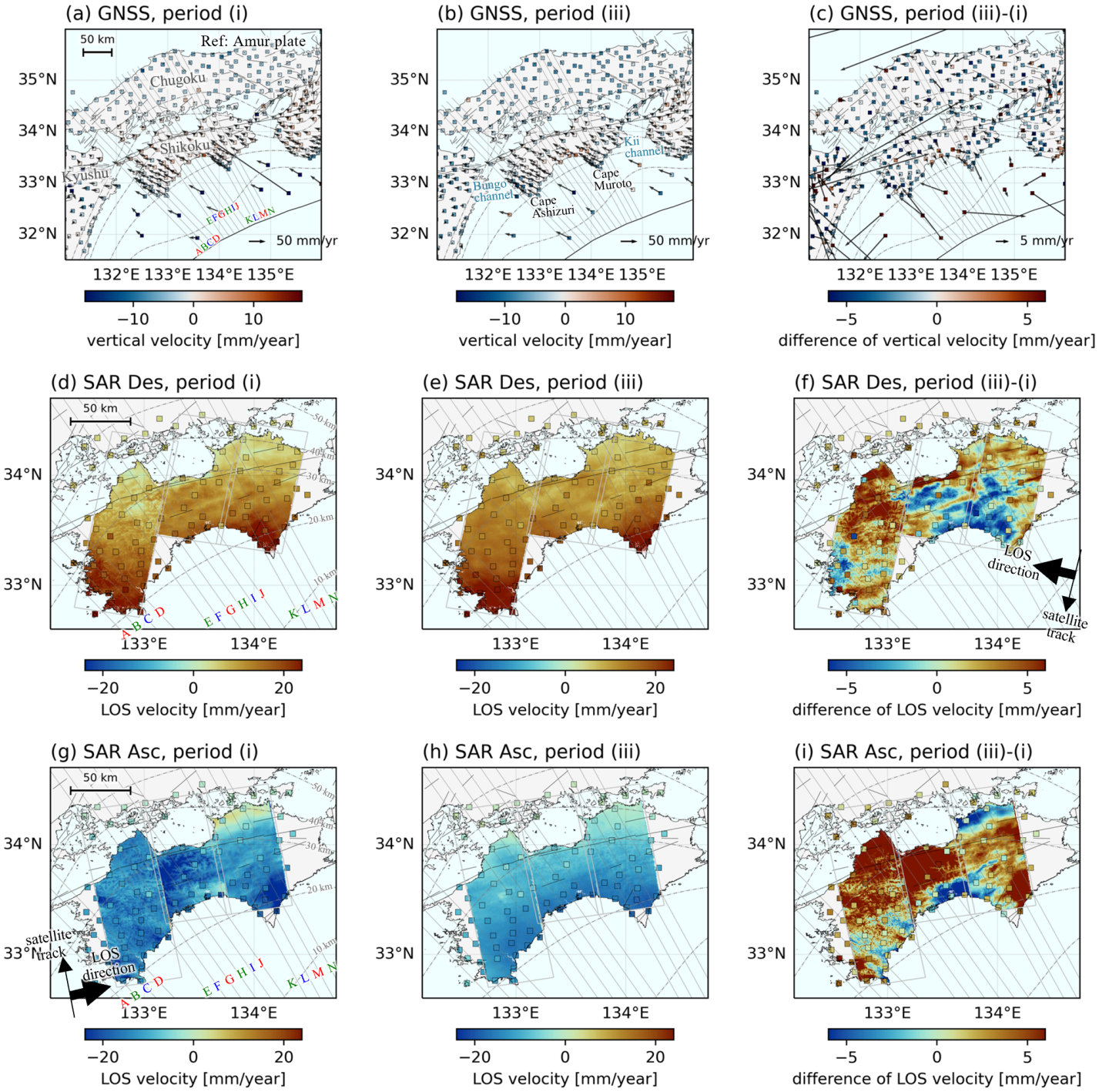


Figure 2

Observed Global Navigation Satellite System (GNSS) and Interferometric Synthetic Aperture Radar (InSAR) velocities. From left to right, columns show velocities in period (i), velocities in period (iii), and their differences. In (a)–(c), black arrows and colored squares indicate GNSS horizontal and vertical velocities, respectively. (d)–(f) and (g)–(i) show line-of-sight (LOS) velocities for descending and ascending frames, respectively. Colored squares indicate GNSS velocities projected into LOS directions. Positive LOS velocities indicate the LOS increase. Trough-normal lines A–N indicate locations of velocity

profiles shown in Additional file1: Figures –S6. We plot active fault traces by thin black lines based on “Active fault database of Japan” (National Institute of Advanced Industrial Science and Technology).

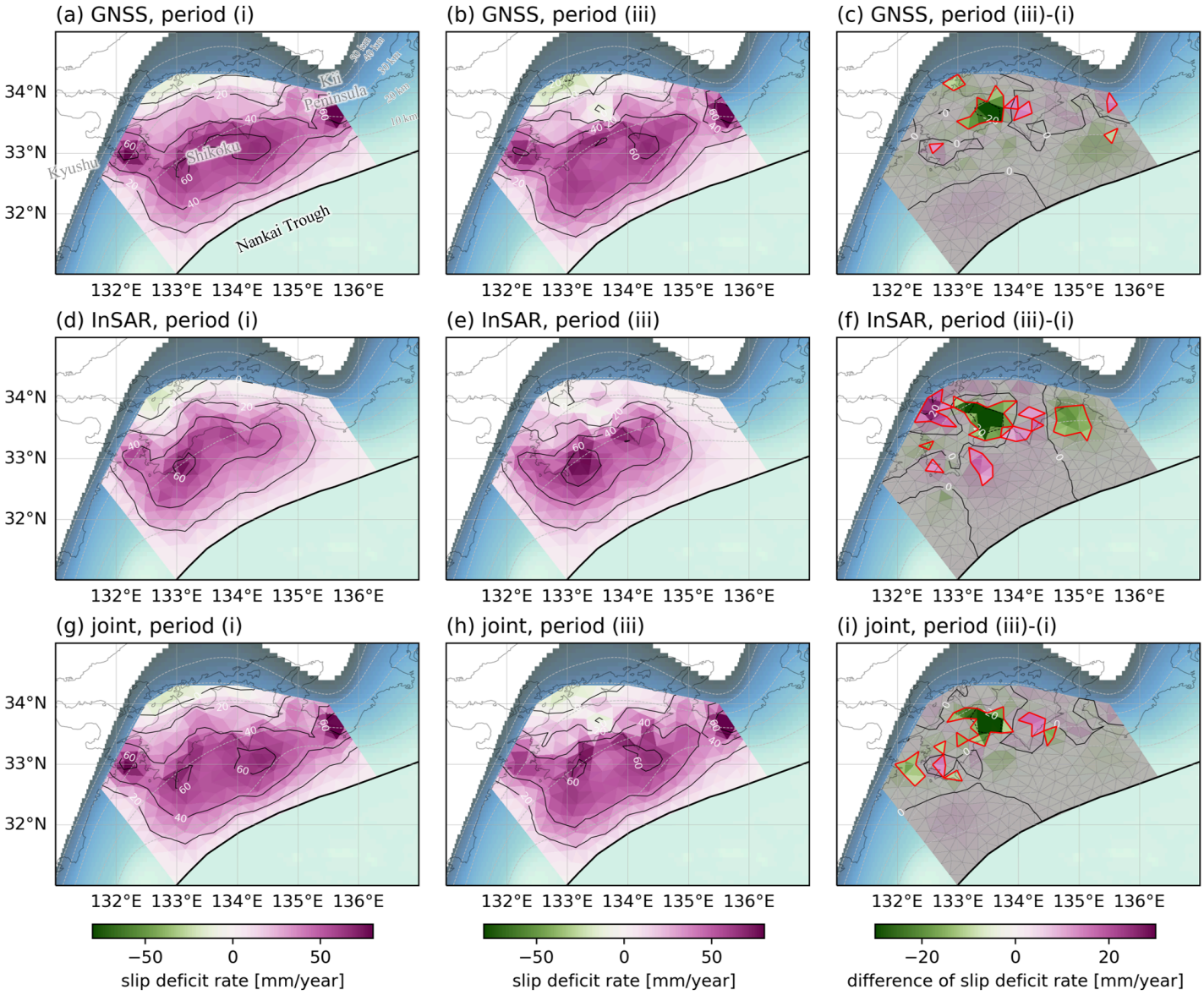


Figure 3

Slip deficit rates estimated from kinematic inversions. Left and center columns show estimated slip deficit rates in periods (i) and (iii), respectively, whereas the right column shows their differences. For (c), (f), and (i), we shade subfaults with smaller changes than the uncertainties in period (i) or (iii), whereas we enclose subfaults with larger changes with red lines. Contours of slip deficit rates are depicted as thin black lines, with an interval of 20 mm/year. Contours for positive values are shown as solid lines, whereas those for negative values are shown as dashed lines.

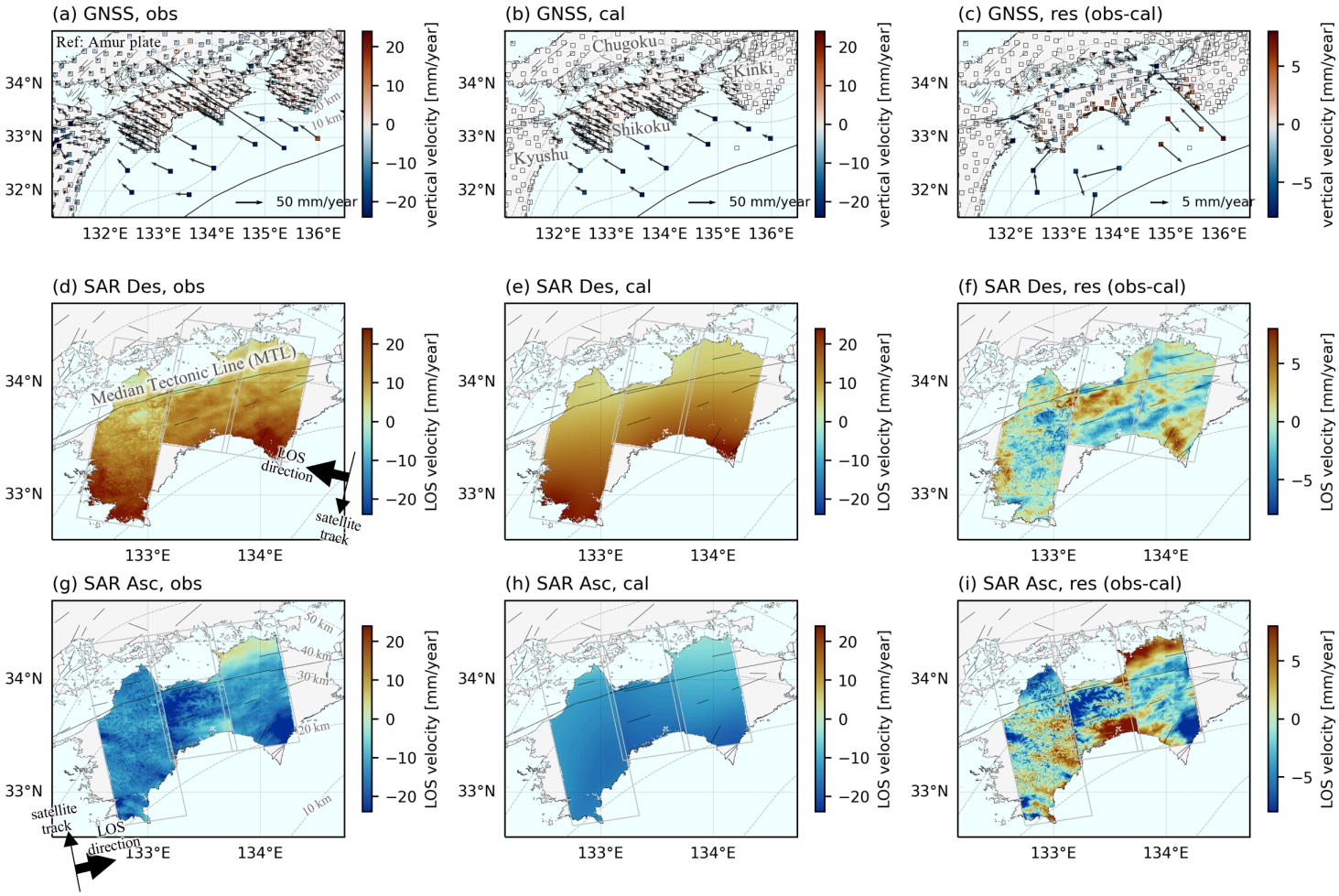


Figure 4

Observed, calculated, and residual velocities for the joint model in period (i). Observed velocities (a), (d), and (g) are same as Fig. a, d, and g. Calculated velocities (b), (e), and (h) are simulated using the joint model (Fig. g). Residual velocities (c), (f), and (i) are obtained by subtracting calculated velocities from observed velocities.

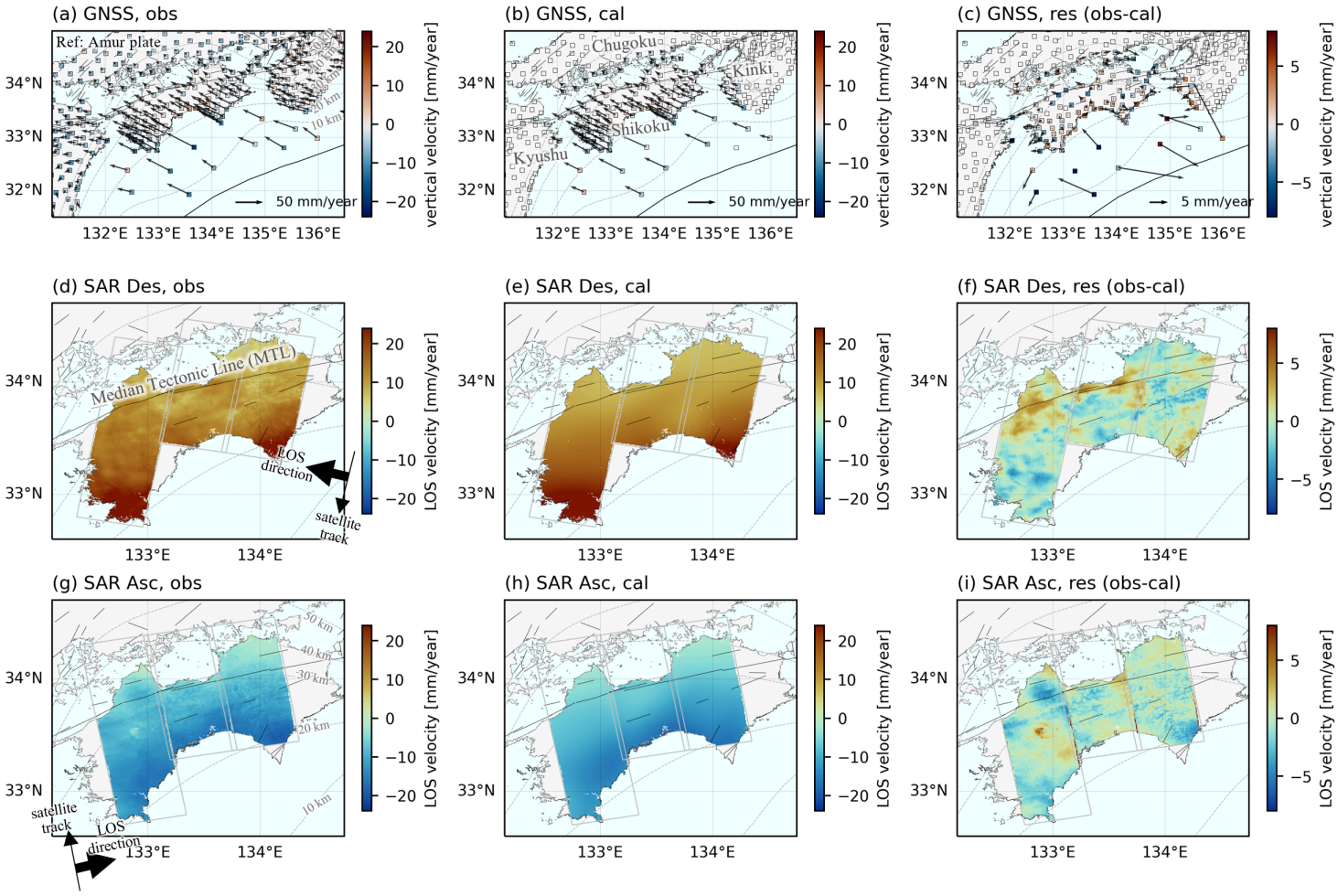


Figure 5

Same as Fig. but for period (iii). Observed velocities (a), (d), and (g) are same as Fig. b, e, and h. Calculated velocities (b), (e), and (h) are simulated using the joint model (Fig. h). Residual velocities (c), (f), and (i) are obtained by subtracting calculated velocities from observed velocities.

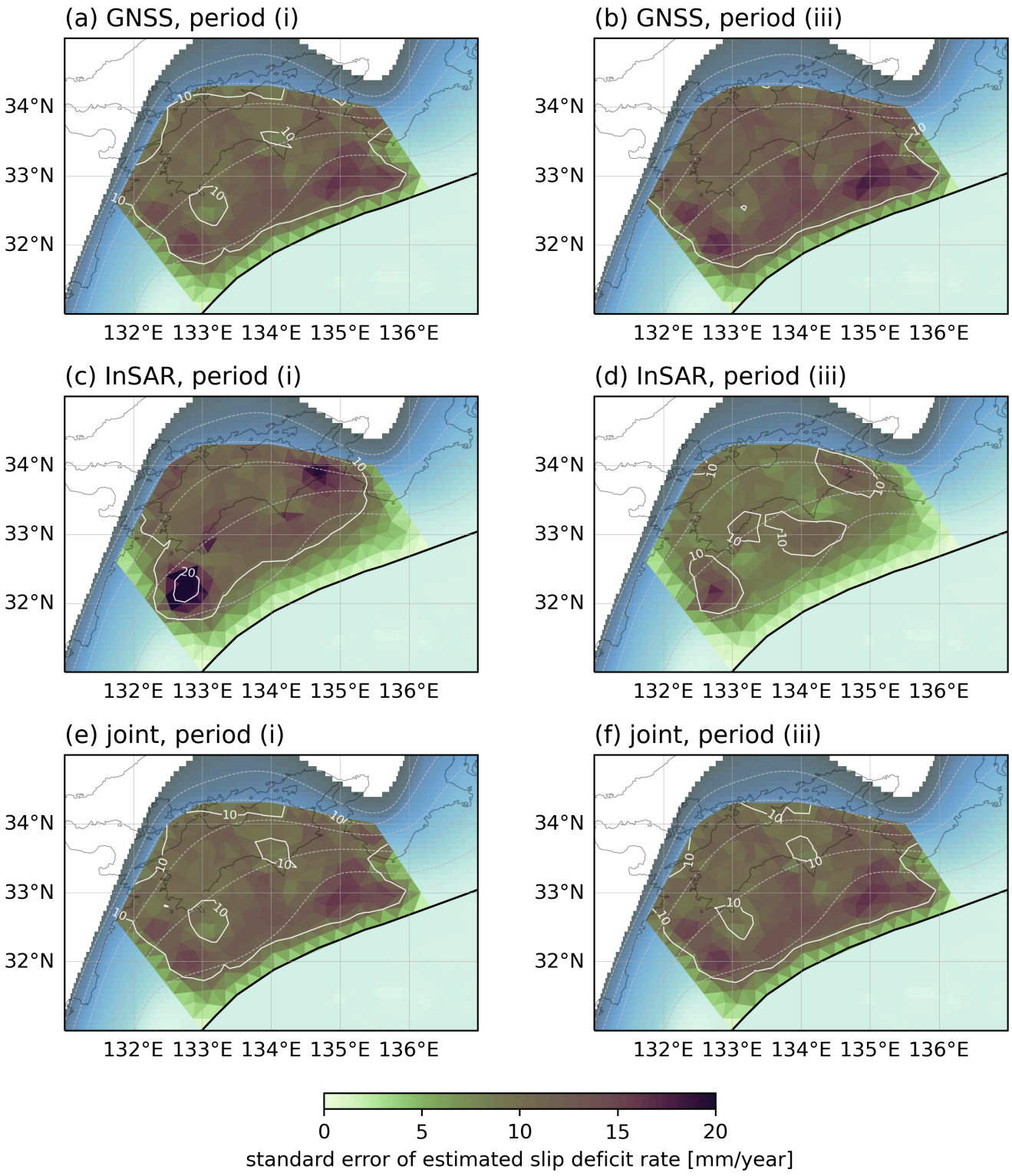


Figure 6

Standard errors of the estimated slip deficit rates. We plot contours of the standard errors as white lines with an interval of 10 mm/year.

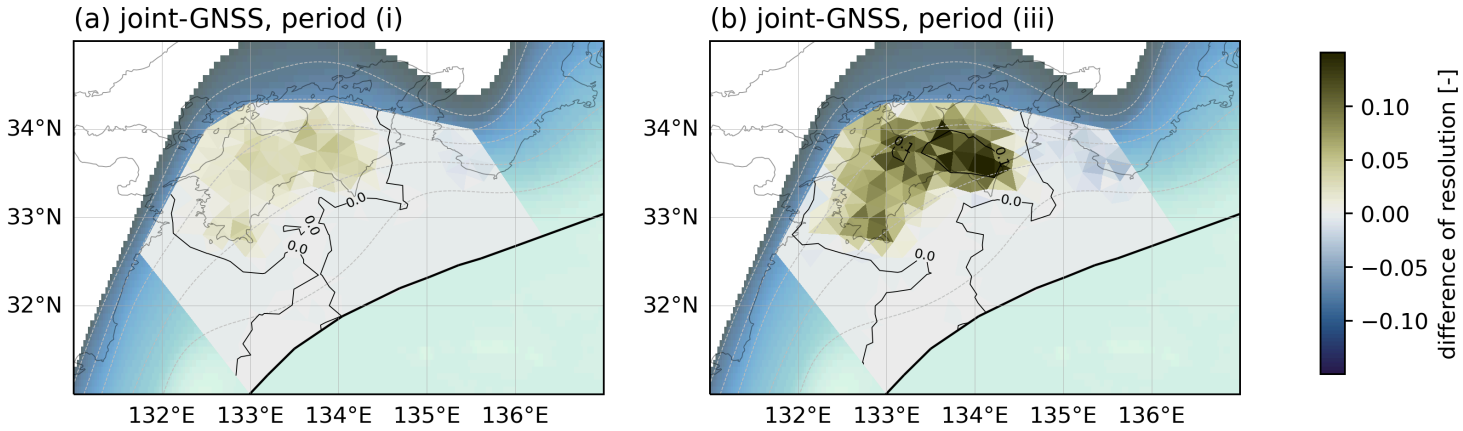


Figure 7

Difference in model resolution between the joint and GNSS models. We plot the differences in the diagonal components of the model resolution matrix, as defined in equation (S23) in Additional file 1: Text S3.

Supplementary Files

This is a list of supplementary files associated with this preprint. Click to download.

- EPSadditionalfile1.pdf
- graphicalabstract.png